# Laser Printed MEMS and Electronic Devices

A.J. Birnbaum,[1] H. Kim,[1] R.C.Y. Auyeung,[1]
N.A. Charipar,[1] K.M. Metkus,[2] S.A. Mathews,[1]
and A. Piqué[1]
*[1]Materials Science and Technology Division*
*[2]NOVA Research, Inc.*

**Introduction:** The vast majority of devices and structures fabricated at the micro-scale and nanometer scale rely on the use of lithographic methods developed decades ago for the microelectronics industry. These methods, while ideal for batch, wafer-based manufacturing, suffer from significant limitations due to material incompatibilities (temperature and chemical resistance), the inability to fabricate based upon nonplanar or curved architectures, and overall process inflexibility.

Interest in digital printing techniques for generating patterns or structures nonlithographically continues to grow. Nonlithographic processes offer relatively low cost, the potential for scalability, inherent flexibility, compatibility with low temperature, and compatibility with nonplanar substrates. Through one such technique, the laser decal transfer (LDT) process developed at NRL, we have demonstrated the fabrication of a range of micron-scale components and devices; these include as-deposited, free-standing structures for sensing/actuation without the use of sacrificial release layers; 3D interconnects; cavity sealing membranes; and multilayered polymer/metal capacitors.

**Free-Standing Structures:** Traditional lithographic techniques almost always rely on removing (etching) sacrificial layers in order to generate free-standing features such as micro-cantilevers for sensing/actuating applications. This etching process represents three to four additional steps in fabrication, as well as the loss in sacrificial material. Using NRL's LDT process in conjunction with specially developed high-viscosity nanocomposites, we have been able to directly print free-standing beams[1] and membranes[2] in an as-deposited manner — that is, without the need for any sacrificial materials or release processes. We have rigorously characterized both the dynamic response of these structures via laser vibrometry, and the mechanical properties via nanoindentation and finite element simulation. Figure 1 shows a schematic of the process and two examples of free-standing components we have produced and characterized.

**Electronic Devices:** Printed electronics have received a great deal of interest in recent years due to their compatibility with low-cost, high-throughput manufacturing techniques such as roll-to-roll processing. The ability to print electronics on nonplanar surfaces is also extremely attractive for DoD-relevant applications and Navy platforms, such as conformal antennae on the wings of an unmanned aerial vehicle (UAV). We have demonstrated the ability to print many types of structures such as 3D interconnects[3] and microscale capacitors[4] via the LDT process. These are shown in Fig. 2. Printing interconnects in a noncontact manner provides the potential for significantly reducing the space required by traditional wire bonding techniques and therefore allows more devices to be embedded within a given area. Furthermore, single laser pulse printing of multilayered laminate structures allows for extremely efficient placement of devices in an "on-demand" fashion. These two abilities applied in tandem serve as key elements for the nonlithographic fabrication of entire circuits.

Finally, in addition to the techniques detailed above, we are developing direct-write processes for printing over large areas in a parallel fashion. Figure 3 shows a laser-printed pattern made by integrating a digital micromirror device (DMD) into our present laser direct-write setup.[5] It is seen that this advancement allows us to dynamically alter the desired pattern to be printed "on the fly." It also shows that instead of having to, for example, build up the "R" one pixel at a time, the entire letter or even word "NRL" can be printed simultaneously from a single laser pulse. This capability is unique to laser printing since no other direct-write technique is capable of printing reconfigurable 3D pixels, or voxels, and represents a significant advance in throughput.

**Moving Forward:** In order to integrate microscale devices and components into existing nonplanar architectures and with nontraditional materials, it is necessary to move beyond the lithographic, wafer-based paradigm. The laser printing methods developed at NRL provide the pathway for providing nonlithographic solutions for small-scale device fabrication without suffering from the drawbacks and limitations of its lithographic counterparts. Furthermore, these laser printing processes lend themselves to being developed for low-cost, high-throughput manufacturing techniques which can prove invaluable for enhancing Navy-relevant technologies.

**References**
[1] A.J. Birnbaum, R.C. Auyeung, K.J. Wahl, M. Zalalutdinov, A.R. Laracuente, and A. Piqué, "Laser Printed Micron-Scale Free Standing Laminate Composites: Process and Properties," *Journal of Applied Physics* **108**, 083526 (2010), doi:10.1063/1.3492708.
[2] A.J. Birnbaum, M. Zalalutdinov, K.J. Wahl, and A. Piqué, "Fabrication and Response of Laser-Printed Cavity-Sealing
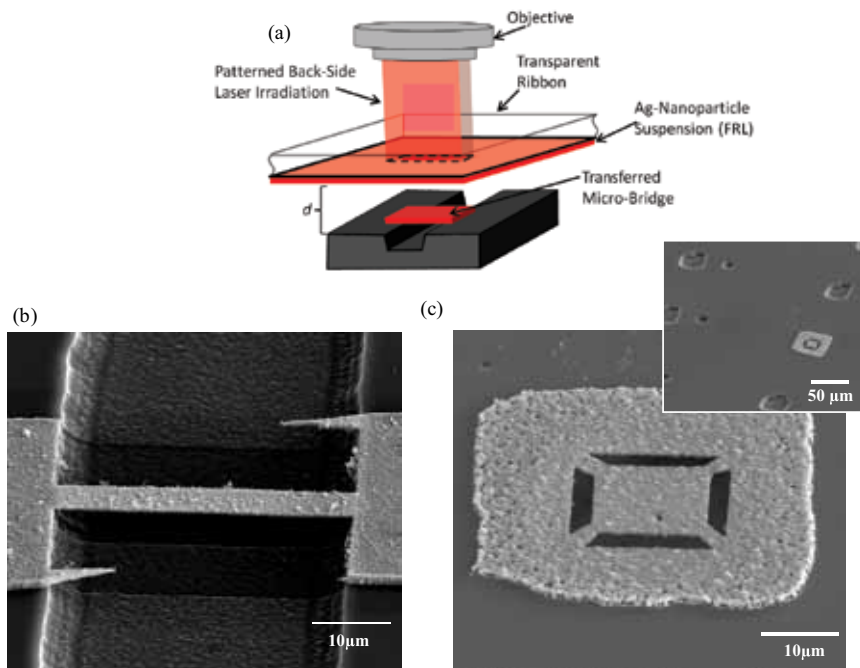
**FIGURE 1**
(a) Schematic of the laser decal transfer process over a prefabricated microchannel. (b) Electron micrograph of a laser-printed micro-bridge over a prepatterned Si channel. (c) Electron micrograph of a suspended, cavity-sealing membrane that has been milled with a focused ion beam for use as a bolometer. Inset is a low-magnification view of the suspended structure and uncovered cavities.
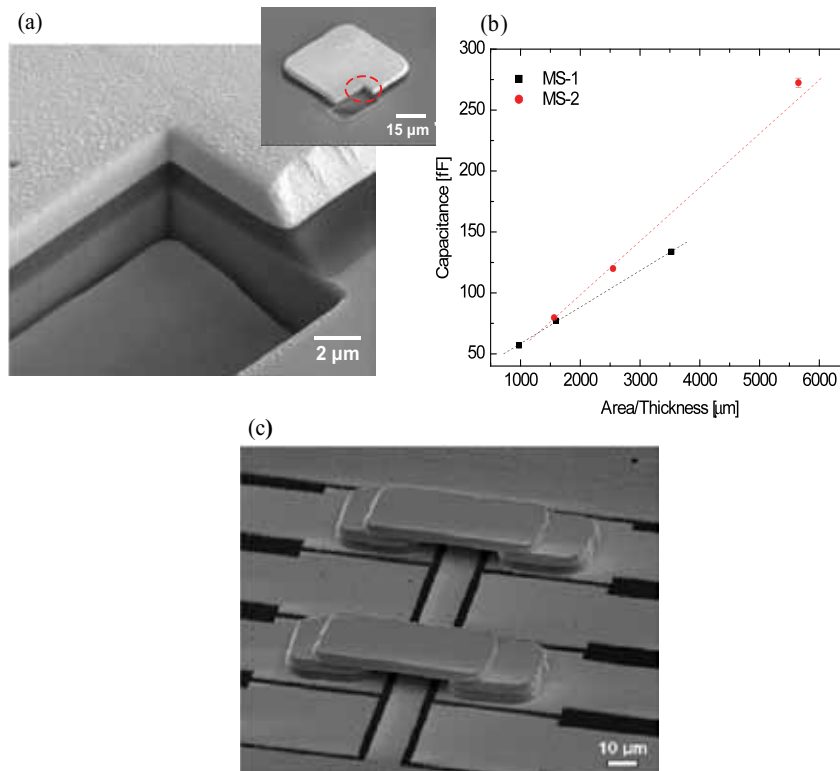


**FIGURE 2**
(a) Electron micrograph of a cross section of a multilayered Ag/polymer stacked hetero-structure capacitor; inset: low-magnification SEM of individual transfer. (b) Capacitance measurements on two different Ag/polymer combinations (MS-1 and MS-2). (c) Electron micrograph of free-standing laser-printed 3D interconnects.
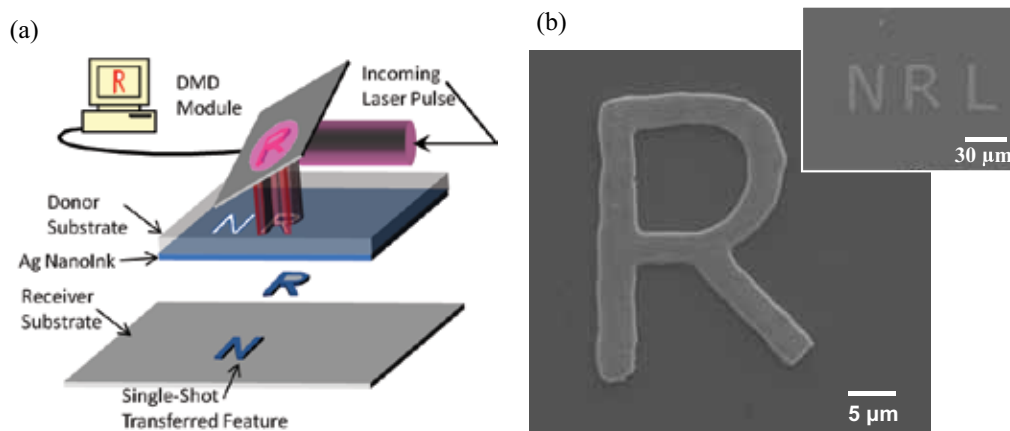
**FIGURE 3**
(a) Schematic of laser printing technique with integrated digital micromirror device. (b) Electron micrograph of parallel laser printed pattern demonstrating quality and resolution of current setup; inset: low-magnification image.

Membranes," *Journal of Microelectromechanical Systems* **20**(2), 436–440 (2010), doi:10.1109/JMEMS.2011.2105251.

[3] J. Wang, R.C.Y. Auyeung, H. Kim, N.A. Charipar, and A. Piqué, "Three-Dimensional Printing of Interconnects by Laser Direct-Write of Silver Nanopastes," *Advanced Materials* **22**, 4462–4466 (2010), doi:10.1002/adma.201001729.

[4] A.J. Birnbaum, H. Kim, N.A. Charipar, and A. Piqué, "Laser Printing of Multi-Layered Polymer/Metal Heterostructures for Electronic and MEMS Devices," *Applied Physics A* **99**, 711–716 (2010), doi:10.1007/s00339-010-5743-8.

[5] R.C.Y. Auyeung, H. Kim, N.A. Charipar, A.J. Birnbaum, S.A. Mathews, and A. Piqué, "Laser Forward Transfer Based on a Spatial Light Modulator," *Applied Physics A: Materials Science and Processing* **102**, 21–26 (2010), doi:10.1007/s00339-010-6054-9.

■

# Microstructural Evolution During Friction Stir Welding of Titanium

R.W. Fonda and K.E. Knipling
*Materials Science and Technology Division*

**Introduction:** Friction stir welding (FSW) has become an important joining technique for aluminum alloys, and promises many benefits in the joining of other alloys. In FSW, a rotating, nonconsumable tool is plunged into and traversed along the joint line of a softer material, generating frictional and deformation-induced heating that softens the surrounding material without melting it, allowing the two sides of the solid metal to be "stirred" together. Since no melting is involved, many problems normally associated with conventional welding are reduced or eliminated.[1]

The microstructural evolution occurring during FSW of titanium alloys can be very complex. The rotating tool introduces shear deformation into the surrounding material, and the heat generated during welding can transform the hexagonal low-temperature α phase to a cubic high-temperature β phase, which reverts back to the α phase during cooling. The heat of welding can also induce grain growth and deformation recovery within the welded regions.

**The Friction Stir Weld:** The weld examined in this study was fabricated in a 12.7 mm (0.5 in.) thick plate of Ti-5111, a near-α titanium alloy with a composition of Ti-5Al-1Sn-1Zr-1V-0.8Mo (in wt %) developed for superior toughness and corrosion resistance in marine applications. The weld was prepared with a simple tool with a truncated conical shape and a narrow shoulder.[2] The original baseplate (BP) microstructure consists of large (~5 mm) prior β grains containing colonies of parallel α laths. By comparison, the weld stir zone (SZ) adjacent to the tool and in the deposited weld consists of fine (~10–20 μm diameter) equiaxed prior β grains containing different orientations of much finer α laths. This microstructure indicates that the peak temperature in the SZ was sufficiently high to fully transform the BP material to β during welding. Separating the BP from the SZ is a relatively narrow (~500 μm wide) thermomechanically affected zone (TMAZ). The objective of this study is to understand the microstructural evolution that occurs across this narrow TMAZ.

**Microstructural Evolution Across the TMAZ:** Since the deformation introduced by the rotating tool is mostly confined to the two-dimensional plane of the plate, the microstructural evolution is best revealed by sectioning the weld terminus in plan-view at the mid-thickness of the baseplate (see Fig. 4(a)). Various regions around the tool exit hole and in the deposited
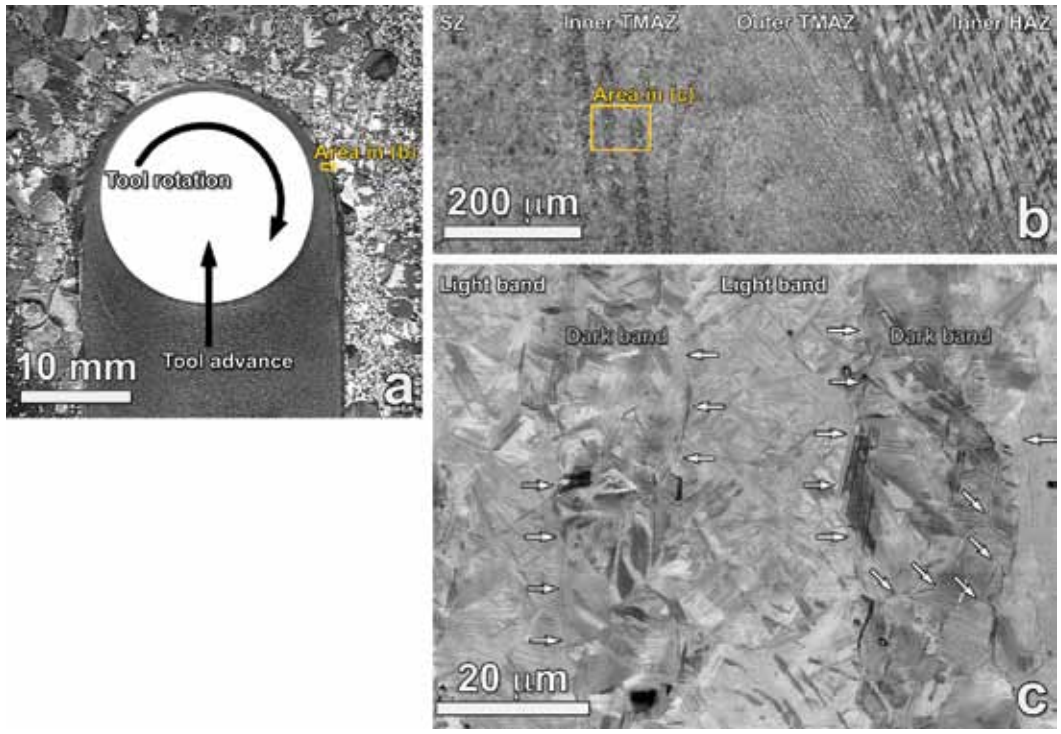
**FIGURE 4**
(a) Optical micrograph of the mid-thickness weld terminus, and backscattered electron micrographs (b) across the transition region and (c) of the microstructural characteristics of the bands.
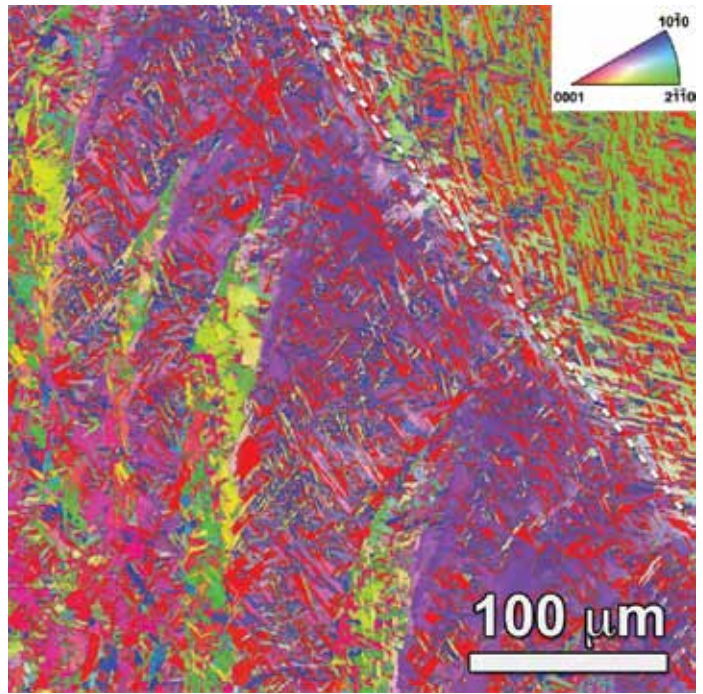


**FIGURE 5**
Orientation map showing the microstructural evolution across the TMAZ.
Colors represent the orientations shown in the inset.

weld were examined, but this discussion focuses on a single region (shown in Figs. 4(b) and 5) that best illustrates the evolutionary processes. In the outer portions of the TMAZ, the shear deformation produced by the rotating tool effects a gradual rotation of the grains. Concurrently, the heat generated during welding partially transforms this region to β, resulting in refined α lath variants (Fig. 4(b)) and new α lath orientations (Fig. 5) that are all related to the original β phase orientation. An abrupt ~10° rotation (dotted line in Fig. 5) in the middle of this region aligns the α phase close-packed directions along the shear direction imposed by the rotating tool.

The inner TMAZ has a banded appearance. Detailed analysis of the bands reveals that the light/purple bands (see Figs. 4(c) and 5) have a microstructure with multiple refined α lath orientations and no prior β grain boundaries, similar to that observed in the outer

the tool, the high temperatures fully transform the material to β, which is readily deformed by the rotating tool. Further from the tool, where the material is only partially transformed to β, there is a gradient of microstructures (and thus flow strengths) resulting from the thermal gradient across this region. Due to this incomplete transformation, deformation of this region is more difficult. Some limited deformation can be achieved through a fragmentation of the microstructure into blocks that individually rotate, establishing a discontinuous lattice rotation in the middle of the TMAZ. This will produce micro-shear bands between the blocks to satisfy the local geometric constraints (Fig. 6(b)). Within the rotated blocks of partially transformed material, continued deformation is constrained by the remaining primary α so that little further rotation occurs along the length of those blocks. However, the localized deformation within the micro-
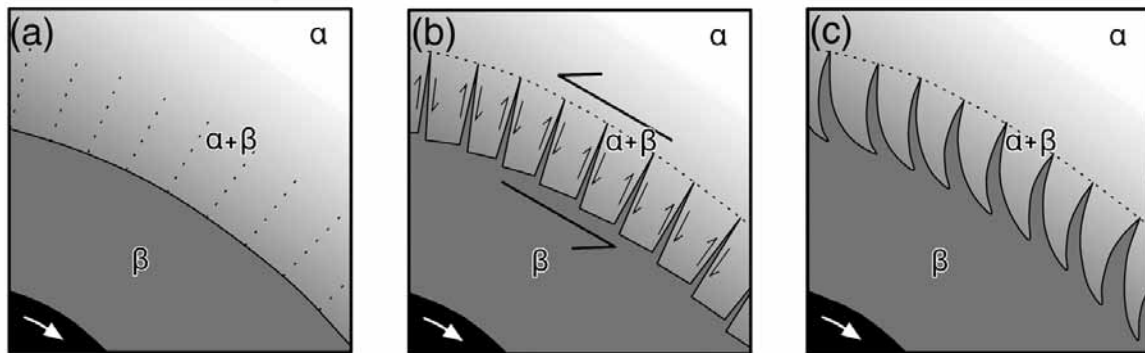


**FIGURE 6**
Schematic of the microstructural evolution during FSW of Ti-5111.

TMAZ. The only significant differences between the inner TMAZ and outer TMAZ are the 10° rotation between them and the larger fraction of refined α laths in the inner TMAZ, indicating a more complete transformation to β before cooling. Thus, these bands are a continuous extension of the original microstructure observed in the BP and outer TMAZ. Alternatively, the dark/green bands have a microstructure of very small (~10 μm diameter) prior β grains containing fine, parallel α laths. The α phase delineating both the prior β grain boundaries (diagonal arrows in Fig. 4(c)) and the interband boundaries (horizontal arrows) demonstrates that this dark/green band completely transformed to β during welding. It is interesting to note that, despite the close proximity of these two bands, the light/purple bands maintain a similar orientation along their length while the dark/green bands exhibit extensive (~110°) rotations along their length.

**Proposed Mechanism:** The mechanism proposed to explain the observed microstructural features and their evolution is summarized in Fig. 6. In the SZ near

shear bands will locally raise the temperature and may fully transform the material in the shear bands to the high-temperature β phase, making it susceptible to extensive (>90°) shear-induced rotations due to the lower flow stress of the β phase. These shear bands expand in width as they experience higher temperatures near the tool, and their microstructure extends continuously into the SZ microstructure near the tool (Fig. 6(c)).

The continuous evolution of these two bands from a common original orientation indicates that the microstructure observed in both bands, as well as in the SZ near the tool, evolved directly from the BP microstructure through a continuous process of transformation, deformation, and recovery.

**References**
[1] R.S. Mishra and Z.Y. Ma, "Friction Stir Welding and Processing," *Mater. Sci. Eng. R* **50**(1–2), 1–78 (2005).
[2] K.E. Knipling and R.W. Fonda, "Texture Development in the Stir Zone of Near-α Titanium Friction Stir Welds," *Scripta Mater.* **60**(12), 1097–1100 (2009).

# Advanced Dielectric Composites with Templated Microstructure through Freeze Casting

E.P. Gorzkowski and M.-J. Pan
*Materials Science and Technology Division*

**Background:** The fabrication of composite dielectric materials to combine the functionalities of constituents in one structure is often limited to very simple configurations, such as randomly distributed particles in a continuous matrix. This is largely due to the lack of an appropriate technique to control the particle assembly process to achieve complex configurations efficiently. In this study, we utilized a freeze casting technique to create a lamellar microstructure with ice as a template. The objective is to fabricate ceramic-polymer composites with a dielectric constant at least ten times higher than that of the conventional random mixture approach. This was achieved by arranging the two phases in an electrically parallel configuration to obtain extremely high permittivity.

**The Freeze Casting Process:** High permittivity ceramic powder is mixed with dispersant, binder, plasticizer, and water to form an aqueous slurry. The slurry is placed in a mold and frozen unidirectionally in a controlled temperature gradient. This is accomplished by placing the mold between two copper rods that are cooled with liquid nitrogen and controlled by band heaters as can be seen in Fig. 7. During freezing, the ice platelet growth front repels ceramic particles to form the interleaving ice/ceramic layered microstructure (Fig. 8). Subsequent freeze drying causes the ice to sublime, thus leaving the desired lamellar ceramic structure. This then may be sintered to improve its mechanical strength or other functionalities. Finally, the lamellar structure is infiltrated with a polymer material to form the desired ceramic-polymer composite.
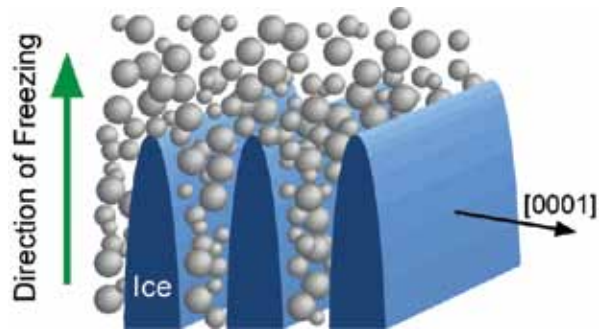


**FIGURE 8**
Schematic of directional freezing process.

**Microstructure:** A typical lamellar microstructure produced by the freeze casting approach is shown in Fig. 9. The platelet thickness is determined by the freezing rate and ceramic volume fraction. In general, the higher the freezing rate, the thinner the platelets and smaller the spacing. Our experimental data showed that, on a log–log scale, the slope of the platelet thickness versus ice growth velocity plot is –0.5, which is consistent with theoretical predictions.[1] The thickness also increases with the ceramic volume fraction up to 60 vol %, beyond which the microstructure breaks down due to insufficient water to push the ceramic out of solution, resulting in dendritic growth.
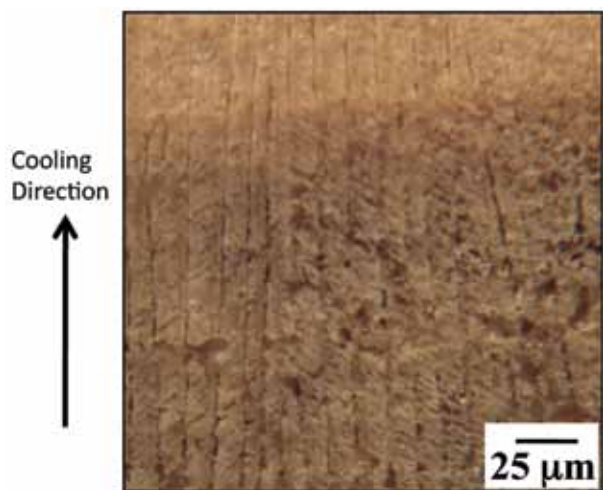


**FIGURE 7**
Directional freezing apparatus.



**FIGURE 9**
Light optical microscopy (LOM) image of a typical lamellar microstructure produced from the freeze casting process.

**Properties and Applications:** The resulting dielectric constant (K) is at least one order of magnitude higher than that of a conventional random mixture, as shown in Fig. 10. The maximum K achieved using barium titanate powder (BT) at 35 vol % is approximately 800, compared to 70 in a random mixture. When PMN-PT (lead magnesium titanate–lead titanate) powder is used, the maximum K increases to 2000 (versus 20 for random). The dramatic increase in freeze-cast samples is due to the connectivity/percolation in the ceramic phase. We showed that there is a linear relationship between the composite dielectric constant and the ceramic volume fraction, and the K approaches the rule-of-mixture prediction (Fig. 11). An unexpected advantage of the dielectric composite is the graceful failure mode. While conventional ceramic capacitors fail catastrophically, our composite self-clears after a breakdown event. That is, it maintains the capability to sustain high voltage loading — a highly desirable characteristic in high K dielectrics. The benign failure mode is attributed to the local clearing of electrode material near the breakdown spot.

The composite also exhibits excellent piezoelectric properties. The piezoelectric coefficient of a 35 vol % lead zirconate titanate (PZT-5A)–epoxy composite was ~250 pC/N, comparable to that of monolithic PZT-5A. Moreover, the 2-2 connectivity of the phases, flexibility in tailoring platelet spacing, and ease of fabrication make the composite a good choice for high-frequency transducer applications. In collaboration with the University of Southern California, a 58 MHz medical transducer for high-resolution imaging was demonstrated successfully.[2]
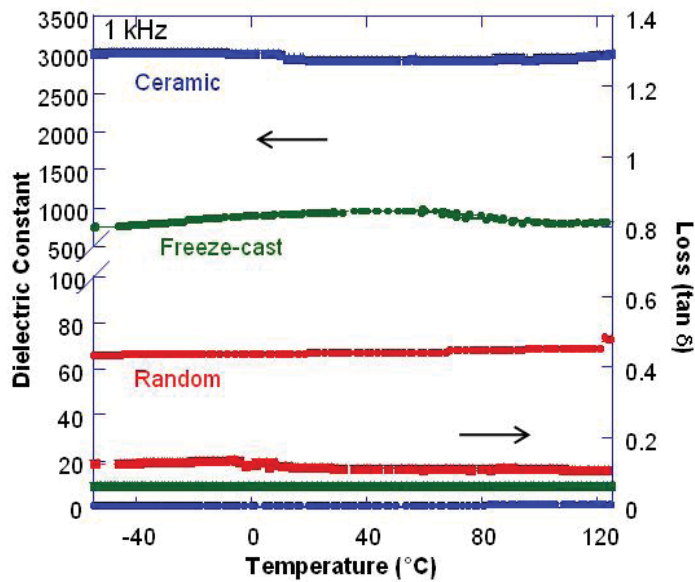


**FIGURE 10**
Comparison of dielectric constant vs temperature data for 35 vol % barium titanate samples created with different processes.
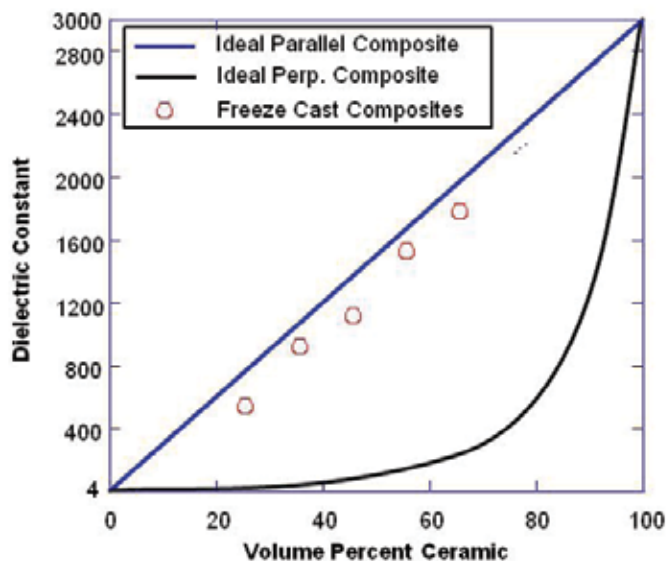


**FIGURE 11**
Dielectric constant vs volume percent ceramic.

**Continuous Casting:** The technique is being adapted to a continuous casting process on a tape caster. The major hurdle to such a process transition is the freeze drying of ice, which requires high vacuum that is difficult, if not impossible, to achieve in a continuous process. Consequently, we switched to camphene as the freeze medium, as it exhibits low melting temperature (45 °C) and readily sublimes at atmospheric pressure and room temperature. The corresponding adjustment of slurry formulation was accomplished successfully. Although the resulting microstructure is not as anisotropic as in the aqueous case, the connectivity of the ceramic phase still leads to respectable permittivity.

**Summary:** This study demonstrated the feasibility, utility, and flexibility of the freeze casting technique for fabricating ceramic-polymer composites. By controlling the freezing of a ceramic slurry, one introduces aligned templates to achieve the desired composite microstructure. The correlation between processing condition, microstructure, and properties was established quantitatively. Most notable, the dielectric constant can be two orders of magnitude higher than that of a random mixture. In addition, the composite's merit as the active element in a high-frequency medical transducer was also demonstrated. The current research focus is to shift the water-based process to a camphene-based process for continuous processing to facilitate future transitions.

[Sponsored by NRL]

**References**

[1] H. Zhang, I. Hussain, M. Brust, M.F. Butler, S.P. Rannard, and A.I. Cooper, "Aligned Two- and Three-dimensional Structures by Directional Freezing of Polymers and Nanoparticles," *Nat. Mater.* **4**(10), 787–793 (2005).

[2] B.P. Zhu, Q.F. Zhou, C.H. Hu, K.K. Shung, E.P. Gorzkowski, and M.J. Pan, "Novel Lead Zirconate Titanate Composite via Freezing Technology for High Frequency Transducer Applications," *J. of Advanced Dielectrics*, **1**(1), 85-89 (2011).

∎

# Novel Air Purification Materials

B.J. White,[1] B.J. Melde,[1] G.W. Peterson,[2] and B.J. Schindler[3]
[1]*Center for Bio/Molecular Science and Engineering*
[2]*Edgewood Chemical Biological Center*
[3]*Science Applications International Corporation*

**Inhalation Threats:** In 2009, the TIC/TIM Task Force released a document focused on toxic industrial chemicals and materials (TICs and TIMs) that pose a threat to the lungs and eyes of deployed troops.[1] The list of compounds is prioritized based on toxic hazard and the likelihood of an encounter. Compounds such as ammonia, sulfur dioxide, nitric acid, and cyanogen chloride are identified in the set of priority inhalation hazards. Traditional air purification materials employed by the military rely on porous carbons. Activated carbon, or activated charcoal, is utilized in a wide range of purification applications including some that are commonly encountered. Home water filtration, for example, relies on a carbon-filled cartridge. Through modification of these types of carbon materials, a number of functional moieties can be combined with the high surface area and adsorptive properties to provide air purification materials with improved characteristics or novel function. Efforts directed at improving the performance of carbon materials in air purification applications, including designing additional capacity for the priority TIC/TIM targets, are under way. Simultaneous efforts seek to provide alternatives to these materials. The effort described here falls into the latter category.

**Novel Reactive Purification Materials:** Our efforts in developing air purification materials have focused on mesoporous organosilicas which are materials that combine organic groups with inorganic silica components to produce sorbents with the properties of both. The materials are rugged and stable, withstanding temperatures of at least 200 °C and exposure to a wide range of chemical conditions. Organosilicate materials are synthesized as shown in Fig. 12. The resulting sorbents consist of particles that have large (~1 μm) pores with small pores (~5 nm) in their walls. The small pores provide the desired high surface area; the larger pores offer reduced resistance to flow and increased connectivity throughout the structure.

The organosilicate materials are the scaffold into which functional moieties are incorporated. One of the major classes of functionalities under consideration is porphyrins. Porphyrins strongly absorb visible light and fluoresce intensely (Fig. 13). They are also well-established electro- and photocatalysts. When compared to proteins and microorganisms, porphyrins are much less sensitive to variations in conditions such as pH and have been shown to withstand temperatures above 150 °C. Modifications to the structure of the porphyrins can be used to alter their binding and catalytic characteristics (Fig. 13). In the novel materials under development for air purification, porphyrins are covalently immobilized within the organosilicate scaffold, providing a high concentration of functional moieties in a low density material.[2]

**Removal of Contaminants:** Targets under consideration for these studies are ammonia, phosgene,
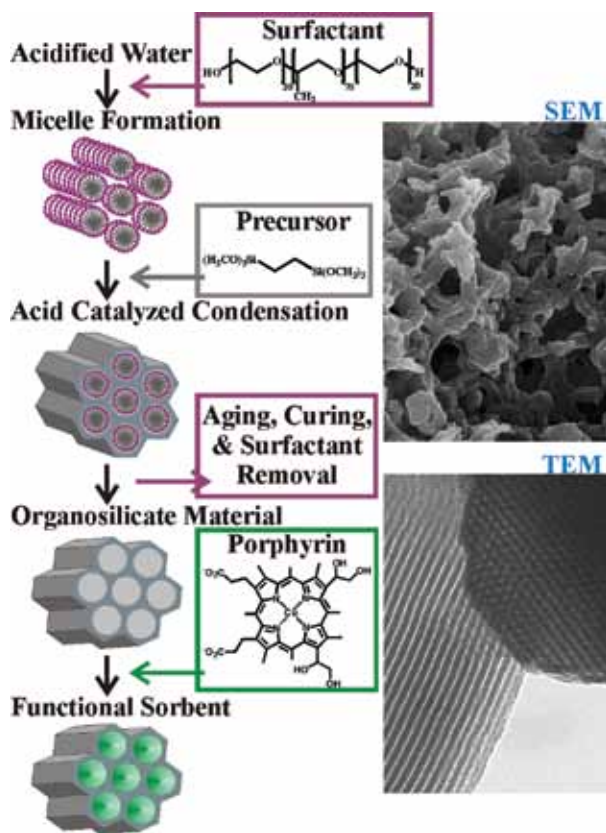
**FIGURE 12**

Synthesis and Morphology. Conditions are established to produce the formation of organized groups of surfactant molecules called micelles. Siloxane precursors, which have alternating organic and silicate groups, are then added to the solution. The surfactant micelles act as a template during condensation of precursors; the organized pore system (7.8 nm pores) is retained when the surfactant is removed. This is seen in the transmission electron microscopy (TEM) image. Phase separation during condensation leads to the formation of large features (~1 µm) in addition to the mesopores. These pores can be seen in the scanning electron microscopy (SEM) image. Porphyrins are grafted onto the surface of the organosilicate materials following synthesis to provide a functional sorbent.

cyanogen chloride, sulfur dioxide, octane, and nitric oxide. Both the spectrophotometric response and the performance of the materials in micro-breakthrough experiments are being evaluated (Fig. 14). A single organosilicate scaffold has been combined with four different porphyrins at a range of loading levels and with varying metal ion incorporation. Using these materials variants, the potential of the porphyrin-embedded organosilicates has been demonstrated, and improved ammonia removal over a control material has been shown. We have also shown that phosgene removal is based on a reactive process rather than a physisorption mechanism. Using a copper porphyrin, the removal of two grams of phosgene per gram of sorbent has been demonstrated in less than five minutes, and repeated

exposure cycles show no decrease in performance. Removal of other targets can be enhanced through the use of functional groups. Primary amine groups, for example, increase the capacity for cyanogen chloride removal, and isocyanate groups increase the capacity for octane removal.

**Applications:** This reactive sorbent technology is being developed with a view toward offering enhanced protective capabilities in next-generation gas masks. The approach taken can, however, be applied to a wider range of air purification applications, such as the removal of formaldehyde from the air systems of buildings. Formaldehyde is one of the common off-gassing products from traditional adhesives and paints. The materials also offer a broader range of applicability
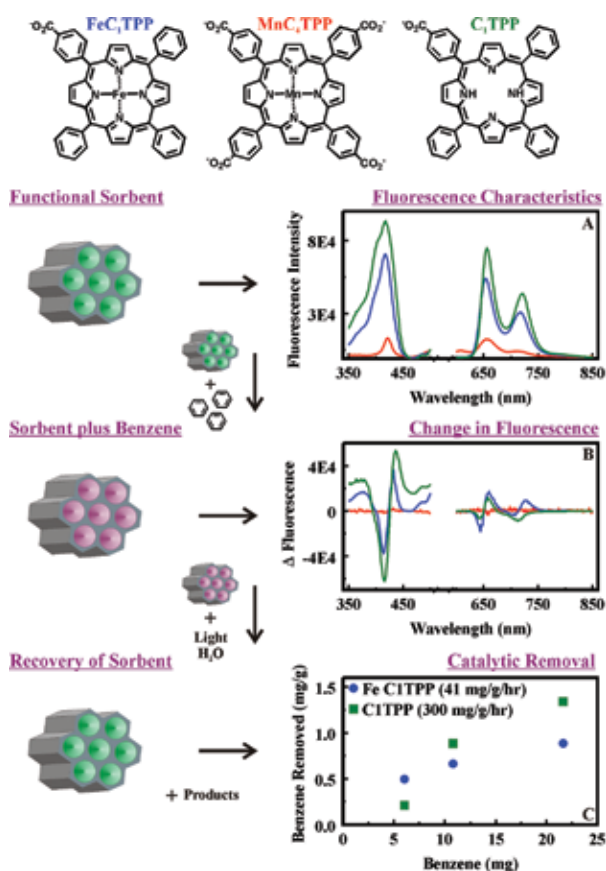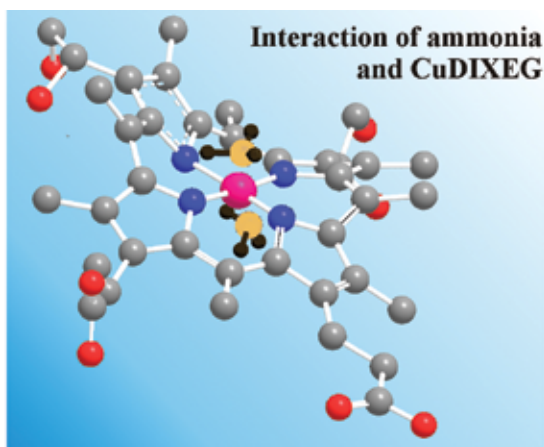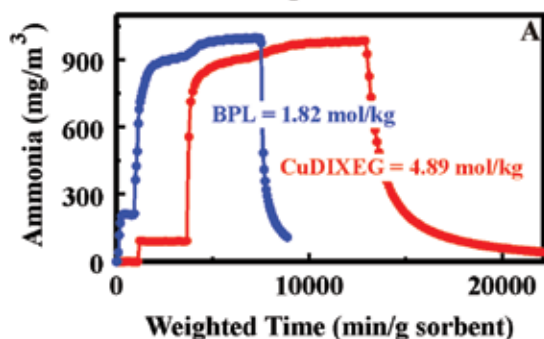


**FIGURE 13**

Porphyrins: Structure and Function. The structures of three representative porphyrins are presented: iron 5-mono(4-carboxyphenyl)-10, 15, 20-triphenyl porphine (FeC$_1$TPP, blue); manganese meso-tetra(4-carboxyphenyl) porphine (MnC$_4$TPP, red); and 5-mono(4-carboxyphenyl)-10, 15, 20-triphenyl porphine (C$_1$TPP, green). Incorporation of porphyrins into an organosilicate material yields sorbents with unique fluorescence characteristics (A), and changes in those characteristics upon target exposure also vary between materials (B). Alteration of the porphyrin structure impacts catalytic activity as shown here for the photoconversion of benzene (C).

## Interaction of ammonia and CuDIXEG

### Ammonia Breakthrough

A

BPL = 1.82 mol/kg

CuDIXEG = 4.89 mol/kg

### Fluorescence Response

B

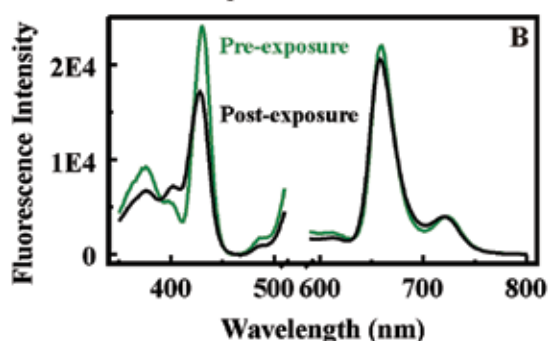Pre-exposure

Post-exposure

**FIGURE 14**
Sorbent Performance. Materials were evaluated as powders in a micro-breakthrough apparatus. The system uses a small sorbent sample packed into a tube, and target is delivered as a gas stream. The stream is continuously monitored for target breakthrough by infrared spectroscopy. (A) The porphyrin-embedded organosilicate sorbent (red) removed more ammonia than the BPL carbon control material (blue, functionalized with zinc and triethylene diamine, TEDA). (B) The fluorescence response to ammonia exposure for a porphyrin-embedded sorbent is also apparent when the fluorescence of the material before (green) and after (black) exposure are compared.

surfaces. The novel sorbents also have potential relevance to sensing applications that utilize absorbance or fluorescence detection mechanisms. Overall, the materials and approaches described here are intended to provide enhanced capabilities in personal protective equipment for use by the warfighter and in chemically resistant coatings for use on military equipment.

**References**
[1] Toxic Industrial Chemical/Toxic Industrial Material Task Force, "TIC/TIM Task Force Prioritization & Application Recommendations," Joint Program Executive Office for Chemical and Biological Defense, http://www.dodsbir.net/sitis/view_pdf.asp?id=REF CBD11_107 FINAL TIC TIM Task Force 060109.pdf, Feb. 2009.
[2] B.J. Johnson, B.J. Melde, C. Thomas, A.P. Malanoski, I.A. Leska, P.T. Charles, D.A. Parrish, and J.R. Deschamps, "Fluorescent Silicate Materials for the Detection of Paraoxon," *Sensors* **10**(3), 2315–2331 (2010), doi:10.3390/s100302315.

through the tunable nature of both the functional moiety and the organosilicate scaffold. Compounds such as traditional nerve agents and pesticides can be targeted through careful design of the organosilicate and selection of the porphyrin catalyst. These types of materials offer the potential for self-decontaminating fabrics and